String method solution of the gating pathways for a pentameric ligand-gated ion channel

Bogdan Lev[a], Samuel Murail[b], Frédéric Poitevin[c,d], Brett A. Cromer[a,e], Marc Baaden[b], Marc Delarue[f], and Toby W. Allen[a,1]

[a]School of Science, RMIT University, Melbourne, VIC 3001, Australia; [b]Laboratoire de Biochimie Théorique, CNRS, UPR9080, Université Paris Diderot, Sorbonne Paris Cité, F-75005 Paris, France; [c]Department of Structural Biology, Stanford University, Stanford, CA 94305; [d]Stanford PULSE Institute, SLAC National Accelerator Laboratory, Menlo Park, CA 94025; [e]School of Health and Biomedical Sciences, RMIT University, Bundoora, VIC 3083, Australia; and [f]Department of Structural Biology and Chemistry, Institut Pasteur and UMR 3528 du CNRS, F-75015 Paris, France

Pentameric ligand-gated ion channels control synaptic neurotransmission by converting chemical signals into electrical signals. Agonist binding leads to rapid signal transduction via an allosteric mechanism, where global protein conformational changes open a pore across the nerve cell membrane. We use all-atom molecular dynamics with a swarm-based string method to solve for the minimum free-energy gating pathways of the proton-activated bacterial GLIC channel. We describe stable wetted/open and dewetted/closed states, and uncover conformational changes in the agonist-binding extracellular domain, ion-conducting transmembrane domain, and gating interface that control communication between these domains. Transition analysis is used to compute free-energy surfaces that suggest allosteric pathways; stabilization with pH; and intermediates, including states that facilitate channel closing in the presence of an agonist. We describe a switching mechanism that senses proton binding by marked reorganization of subunit interface, altering the packing of β-sheets to induce changes that lead to asynchronous pore-lining M2 helix movements. These results provide molecular details of GLIC gating and insight into the allosteric mechanisms for the superfamily of pentameric ligand-gated channels.

pentameric ligand-gated ion channel | ion channel gating | string method molecular dynamics | allosteric modulation | pH activation

Pentameric ligand-gated ion channels (pLGICs) control synaptic neurotransmission by converting chemical signals into electrical signals, enabling complex signal processing that underlies nervous system function. This signal transduction is achieved by an allosteric, Monod–Wyman–Changeux mechanism (1), where selective binding of an agonist, such as a neurotransmitter, leads to a global protein conformational change that opens an ion-conducting pore across the nerve membrane. Over 50 years of study has given us in-depth knowledge of the physiology and pharmacology of pLGICs (2). However, it is only in the past few years that we have begun to see what these proteins look like in atomic detail (3–13), and we now have an opportunity to describe the mechanisms of pLGIC function at the molecular level.

The pLGICs are made up of five identical or homologous subunits, each composed of an N-terminal β-sheet sandwich extracellular domain (ECD) followed by a four-helix transmembrane domain (TMD) (Fig. 1A). Between the ECD subunits are the binding sites for agonists, formed from seven segments or "loops": A–C from the principal or (+)-side subunit and D–G from the complementary or (−)-side subunit, with loop C forming a lid between the bound agonist and the surrounding extracellular medium. The binding of a ligand under loop C is thought to change intersubunit contacts and alter the internal structure of each subunit. How this perturbation is communicated through the "gating interface" at the boundary between the ECD and the TMD to the distinct ion-conducting pore formed by the pentamer of M2 helices in the TMD is not completely understood.

To shed light on this transduction process, one must observe the conformational changes that occur between active/open (O)

and resting/closed (C) forms. Fortunately, X-ray crystal structures for both forms of the pH-activated GLIC channel (4, 6, 7) have been solved. Structures of multiple states of the channel GluCl have also been solved (3, 9), with generally similar conformational changes, but with differences in the TMD that may signify variability in the family, or that could be artifacts due to the use of antibody fragments or the large antiparasitic ivermectin to trap the GluCl O structure (3). Moreover, O and C structures of α1-Gly receptor (GlyR) have been solved with cryo-EM (10, 11), and also solved in the presence of ivermectin or the inhibitor strychnine. The ELIC (8), β3 GABA$_A$ receptor (GABA$_A$R) (13), 5-HT3 (12) and α4β2 nACh receptor (nAChR) (14) channels, solved in one state, provide valuable comparisons to explain receptor diversity but do not offer consistent end points for studies of gating. We therefore focus on pH-activated GLIC, with O and C structures solved under conditions that differ only by the presence of agonist (protons). GLIC transitions from maximally open at pH 4.6 to fully closed at pH 7, with a pH of half-maximal activation (pH$_{50}$) of ~5.3 (4), due to protonation sites within the ECD (15), mimicking agonist binding. High-resolution structures of GLIC, Protein Data Bank (PDB) ID codes 3EAM and 4HFI (being very similar), have been demonstrated to represent the O state with simulations of ion occupancy in the pore (16), and by double electron–electron resonance (DEER) spectroscopy (17). Although a high-resolution structure has also been solved for a locally closed (LC; activated ECD, closed TMD) state with cross-links or single-point mutations (H235F, E243P) near the gating interface (5), we consider only WT O and C forms for investigation into pathways based on end points of the gating transition.

Significance

High-resolution structures of pentameric ligand-gated ion channels have created an opportunity to discover the mechanisms of rapid synaptic transduction in the brain. This study describes the mechanisms of allosteric channel gating using string method simulations, applied to a complete atomistic ion channel, combined with a transition analysis approach to extract free-energy surfaces from swarms of trajectories. We reproduce pH-modulated activity of the channel, identify the molecular interactions associated with interdomain communication, and quantify the energetics of the gating process. These results provide general mechanistic understanding of the function of pentameric ligand-gated channels, with potential applications in the design of improved anesthetics, neuromodulatory drugs, antiparasitics, and pesticides.
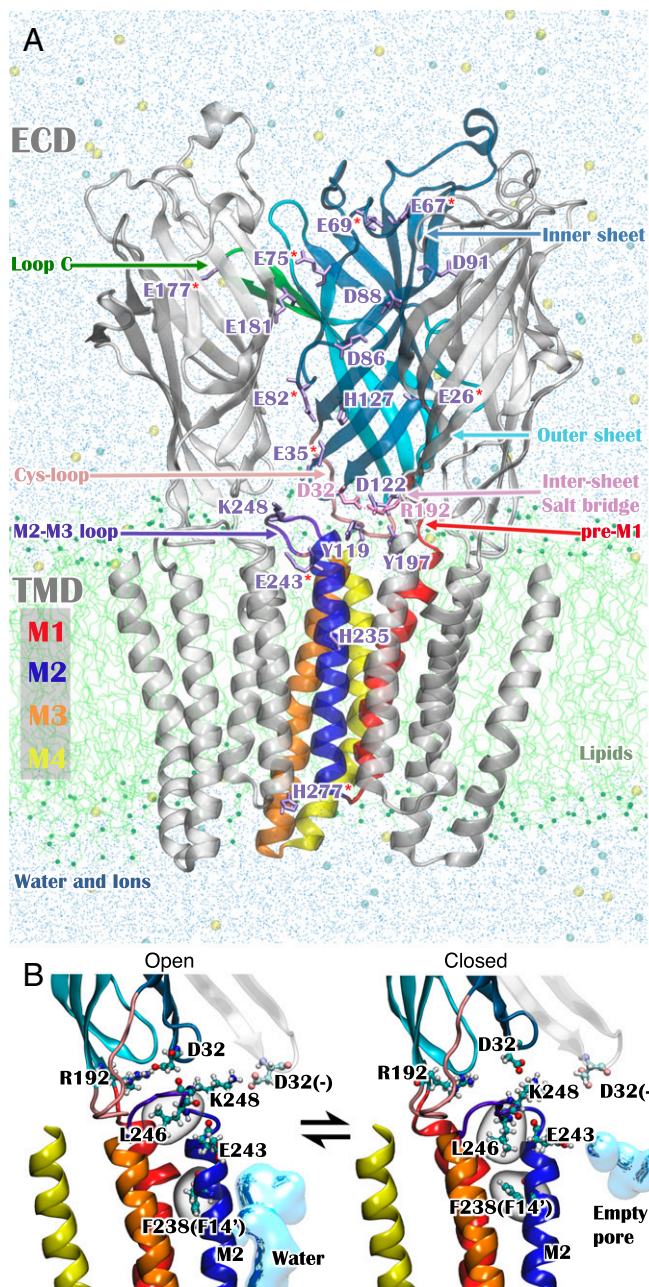
Fig. 1. (*A*) Atomistic simulation system showing GLIC protein as ribbons (nearest two subunits removed, with the rear subunit shown in color and with the inner and outer β-sheets, loop C, Cys loop, D32-R192 salt bridge, TMD helices M1–4, pre-M1, and M2-M3 indicated) in a hydrated lipid bilayer (chains shown as green lines, water shown as blue dots, and NaCl shown as yellow/cyan balls). Important protein side chains are drawn with sticks, with titrated residues identified (*). (*B*) Gating interface changes during string simulations, showing the D32-R192 salt bridge breaking, the L246-P247-K248 motif flipping, K248 interaction changes from E243/D32(−) to D32, and wedging of L246 between M2 and M3 in the vicinity of F14′ (F238). Disappearance of a continuously water-filled pore is illustrated with a blue surface (also Movie S1).

Our aim is to describe the molecular events and energetics of GLIC pH activation, communication between separate ECD and TMD domains, and the opening/closing of the ion-conducting pore. Atomistic molecular dynamic (MD) simulations, over long (microseconds or longer) time scales, offer structural refinement in a native-like membrane environment and opportunities for observing conformational changes as a result of the addition or removal of agonists (18–22). Even simulations on relatively short time scales can be informative in terms of the quaternary and tertiary changes in the different domains of pLGICs (e.g., refs. 20, 21). However, in general, unbiased simulations are likely to yield incomplete or anecdotal evidence, due to the time scales of gating being comparable to or exceeding simulation times. Instead, we directly model the gating process here using a "swarms of trajectories" string approach (23, 24). We refine guess trajectories between O and C states to converge on the minimum free-energy pathways for gating using a large number of simulations to explore conformational transitions (24). This significant demand on computational resources, beyond typical MD simulations, is needed to ensure optimization of conformational changes. We have devised an analysis of millions of transitions to obtain free-energy surfaces that reveal pH-dependent activity, activation pathways, intermediate states, and interdependencies of conformational variables that help to explain allosteric communication in pLGICs.

Results and Discussion

Conformational Changes Along the Activation String. We have carried out a swarm-based string method calculation that exploits large numbers of short simulations to explore configurational space and converge on the minimum free-energy pathways of activation (23–25) (*Methods*). The procedure requires selection of a small set of collective variables that account for the dominant protein conformational changes. The crystallographic C and O GLIC states have previously revealed a marked radial spreading (also called blooming) and tangential twisting of the ECD, leading to a structurally diverse C state (4). The ECD β-sandwich is composed of inner and outer sheets, with connecting loops (Fig. 1*A*) that are thought to contribute to signal communication (26). Altered packing against these β-sheets is thought to lead to expansion of the lower β-sandwich, evidenced in GLIC by the breaking of the D32-R192 salt bridge (4). Although D32 is not strictly conserved (*SI Appendix*, Fig. S1), this bridge is part of a largely conserved triplet, D32-R192-D122, of which R192-D122 is highly conserved and essential for function (27, 28), and mutation of D32 in GLIC causes loss of function (28). Breaking of D32-R192 and β-sandwich expansion likely cause changes that influence interdomain communication via deflection of the pre-M1 R192 residue (29–31), or through noncovalent interactions, as indicated in Fig. 1*B* (observed in string simulations and described below). Finally, the TMD pore is narrowed in the C state associated with M2 helix movement inward and away from its partner M1 helix in the neighboring [complementary or (−)] subunit (4), leading to pore constriction via hydrophobic residues (32) and expelling of water (Fig. 1*B*). These observations have guided our selection of variables, as outlined in *Methods*.

Following targeted MD simulations between O and C states at low (pH 4.6) and high (pH 7) pH to provide initial guess pathways, string optimization in the full dihedral space of the protein was first carried out, allowing statistics to guide reduction of correlated variables (*SI Appendix*, Fig. S2). The final choice of 35 variables (seven per subunit), as defined in *Methods*, is illustrated in Fig. 2 *A–C*. Optimizations in this 35D space were carried out to convergence, with two independent strings for each pH. We begin here by reporting the approximate order of conformational changes along these strings, each consisting of a set of 42 "images" distributed between the O and C states (40 images plus two fixed end points), as summarized in Fig. 2*D* for pH 4.6 (independent strings are shown in *SI Appendix*, Fig. S3 *A* and *C*, results for pH 7 provided in *SI Appendix*, Fig. S3 *B* and *D*, and raw data are shown in *SI Appendix*, Fig. S4). These image-image trends only provide a guide to the sequence of changes, subject to fluctuations in a broad energy well (described below), in contrast to the quantitative statistical analyses to follow.

At low pH, following the initial rapid progress in ECD changes from O (Fig. 2*D*, image numbers to the left) to C (Fig. 2*D*, image numbers to the right), we see changes in TMD variables (M2 collapse

www.manaraa.com
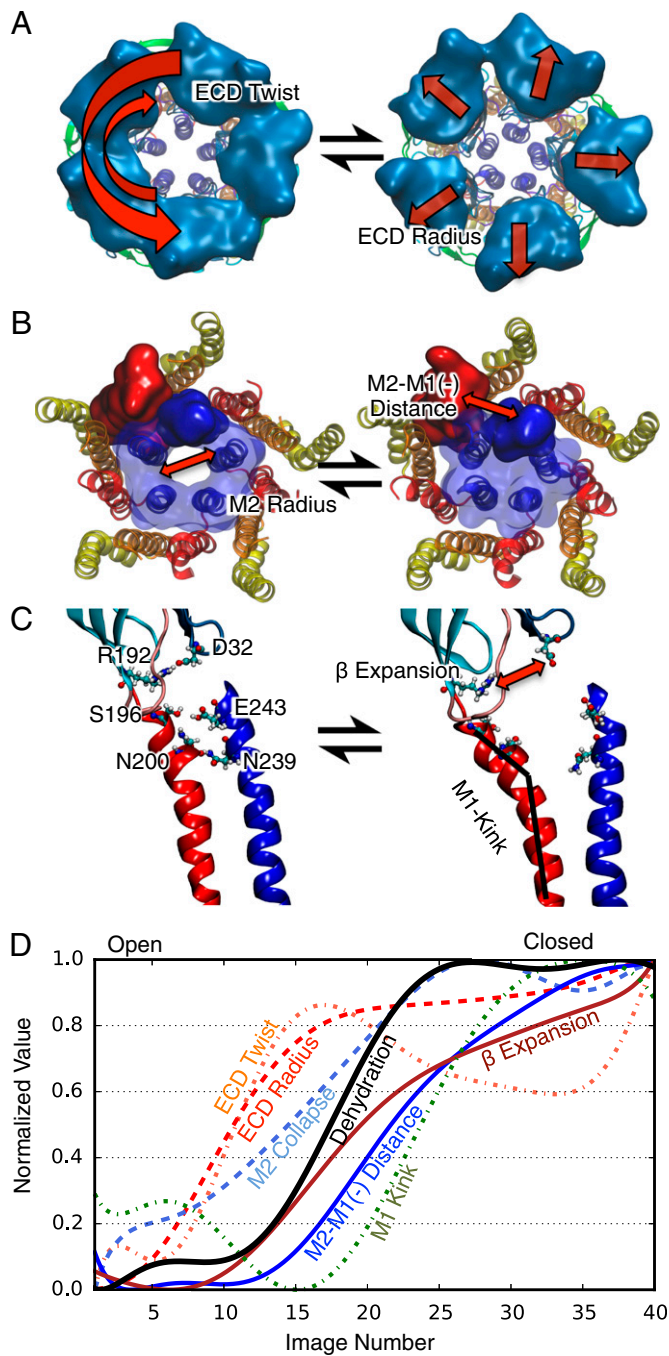
Fig. 2. (*A–C*) Structural changes between O (*Left*) and C (*Right*). (*A*) ECD radius (Movie S2) and ECD twist (rounded arrows indicating relative twist with TMD). (*B*) M2 radius (Movie S3) and M2-M1(−) distance (M2 shown in blue and M1 shown in red; Movie S4). (*C*) Lower β-sandwich expansion (Movie S5) and M1 kink [also illustrating changing M2 interactions with M1(−)]. Pore dewetting is shown in Movie S6. (*D*) Normalized changes for pH 4.6 against image number (pH 7 is shown in *SI Appendix*, Fig. S3, and raw data are shown in *SI Appendix*, Fig. S4). Variables that decrease from left to right are plotted as dehydration (1 − hydration) and M2 collapse (1 − M2 radius).

and dehydration), lower β-sandwich (β-expansion), M2-M1(−) distance, and M1 kink (with all variables normalized). It thus appears that ECD expansion and twisting are required before other changes can occur to close the channel. The contracted ECD can be considered as a stabilizing "cap" on the O state that needs to be released for channel closing. The reverse process (C to O) does not

experience the same order, because the C-state ECD is already expanded and twisted, with the dynamic ECD allowing for multiple concurrent changes during opening. Note that the high ECD twist at image 40 is due to holding the string end at the initial C structure, whereas the optimized C state, spanning a range of images, has a reduced level of twist, such that the majority of ECD changes occur late (to the left) in the opening process. In this case, β-contraction is the initial step, preceding TMD transitions, and the last (or slowest) change then involves the ECD. At high pH, the process is similar (*SI Appendix*, Fig. S3 *B* and *D*). These observations suggest ECD change is the trigger for global change during closing, whereas β-contraction is the trigger in channel opening.

Estimates of the reversible work to change a string variable from the O to C state (*SI Appendix*, Fig. S4, *Right*) were obtained from forces during constrained trajectories (*Methods*). These profiles reveal that several kilocalories per mole are required to move from the O state to the C state at low pH, but that changes become more favorable at high pH. This equilibrium shift is seen in each profile, yet it is the ECD that contains the protonating sites that drive gating, as we now examine.

Quaternary ECD Changes Driven by Protonation Sites. As the protein changes from O to C at pH 4.6, ECD spreading and twisting occur steeply (Fig. 2*D*). Twist increases from 12.7° to 16.7° midway along the coordinate, overtwisting before dropping to 15.2° in the C state, with similar changes at high pH (*SI Appendix*, Fig. S4*A*). A small overspread can also be seen in two of four independent strings in *SI Appendix*, Fig. S4*B*. This finding may suggest an unlocking and alignment of the ECD before interactions can be formed that stabilize the C state.

GLIC has a number of titratable residues expected to change protonation states between pH 4.6 and pH 7 (*Methods* and *SI Appendix*). Although the only histidine determined to change state was H277, this residue, at the base of the TMD, is not expected to drive ECD changes. Residue H127 was found to be protonated at both pH values, whereas H235 was always deprotonated. No basic residues or aspartates were determined to change state, with pH sensitivity coming exclusively from glutamates at the ECD subunit interface, including E26, E35, E75, and E82 (and E243 at the top of M2 in the TMD; Fig. 1*A*); E177 on loop C, which forms the usual agonist binding lid; and two other loops (E67 and E69) exposed to solvent.

The net subunit charge changing from +4e to −5e with pH results in a long-ranged Coulombic expansion force. Although changing interaction energies have been observed within and across subunits as a function of pH (*SI Appendix*, Fig. S5*A*), such analysis is limited in its ability to explain the influence of particular residues on conformational change. To quantify the contributions to ECD spreading directly, we have computed a residue decomposition of electrostatic reversible work in Fig. 3*A* (summarized in Fig. 3*B* for pH 7–pH 4.6). Given the approximate treatment of electrolyte screening (*SI Appendix, Supporting Analysis*), these results provide a guide to whether residues assist or oppose gating with pH. Residues E35 and E75 (as well as E69, despite screening) assist ECD spreading, with increased pH driving the channel to the C state. Residue E243, although in the TMD, also assists in ECD spreading through repulsive forces on the neighboring subunit (including with E243 itself). Of particular note is that E75 reverses its effect with pH (contracting at low pH and expanding at high pH), owing to repulsive partners on the complementary subunit (notably D88 and D91). E75 is part of the largely conserved WXPD/E motif on loop A, important for loop A/B interactions that create an orthosteric site in other pLGICs (26). Rather than leading to an intersubunit pocket, E75 deprotonation appears to control ECD spread through its exposure to the complementary subunit face. Residue E82 is well screened and has little effect, whereas E177 and E26 oppose ECD spreading and help keep the channel open at high pH. The role of E177 was unexpected, because it sits at the periphery, but it lies on loop C, which caps agonists in eukaryotic neurotransmitter pLGICs, with protonation potentially mimicking

www.manaraa.com
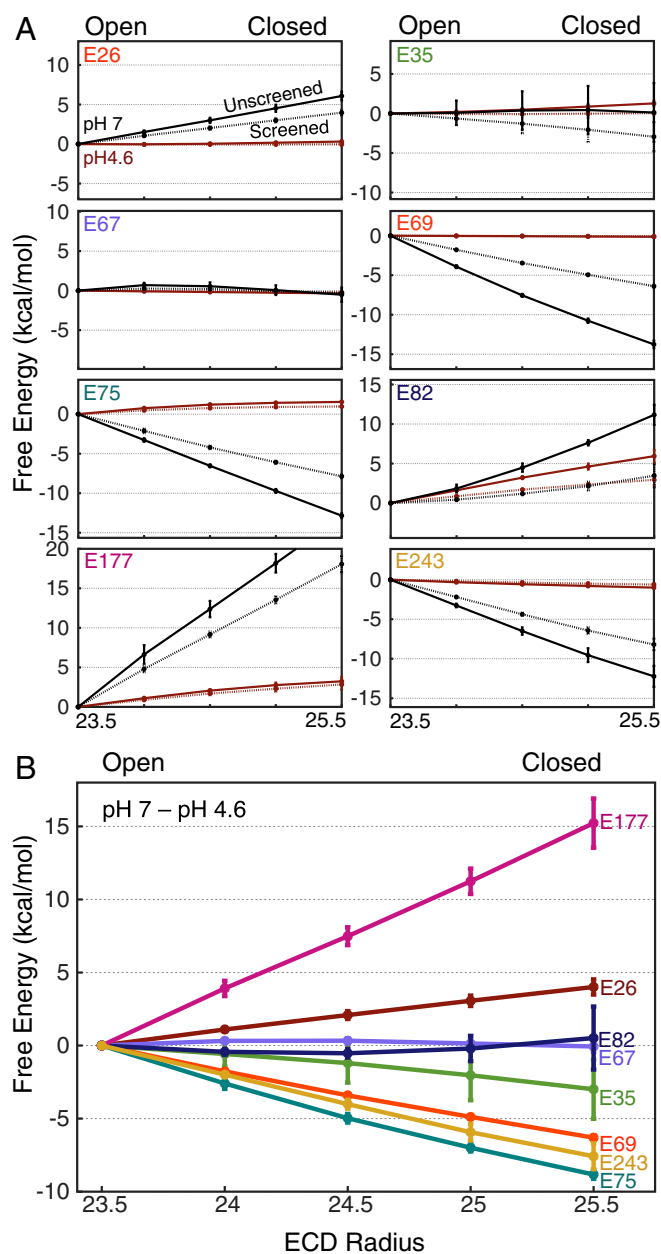
Fig. 3. Mean force decomposition of ECD spreading work, based on electrostatic interaction forces between individual residues (that change protonation state) and other subunits. (*A*) Work contributions for individual residues for pH 4.6 (red) and pH 7 (black), with unscreened electrostatics shown as solid curves and screened electrostatics shown as dotted curves. (*B*) Comparison of all screened electrostatic work contributions (pH 7 to pH 4.6).

agonist binding through attractive intersubunit interactions, consistent with the role of loop C in proton activation (33).

Rearrangements at the ECD–TMD Interface and TMD Pore. ECD spreading and twisting alter the packing against the β-sheets, which extend down to the gating interface, signified by lower β-sandwich expansion [separation of β-sheets in the vicinity of R192 (pre-M1) and D32 (loop 2) from ∼11.5–13 Å; *SI Appendix*, Fig. S4*D*] and the breaking of the R192-D32 salt bridge upon channel closing. This movement deflects the pre-M1 main-chain linkage from ECD to M1. As a result, we observe M1 to kink at P204, increasing its value by ∼5° upon closing (*SI Appendix*, Fig. S4*G*), likely influencing pore collapse. Indeed, M1(−) interacts

favorably with M2 in the O state, through H-bonds N200-N239 and S196-E243, but not in the C state (Fig. 2*C*).

The expansion of the lower β-sandwich alters the proximity of D32 to key TMD residues (Fig. 1*B*), influencing the M2-M3 loop. The behavior of this loop is important for GLIC and other pLGICs (9, 10, 20, 28), and its crystal conformation may have been influenced by nearby lipid and detergent molecules (4, 6). Based on string simulations, we observe distinct molecular events, in addition to overall movement of the segment. Fig. 1*B* (also Movie S1) shows flipping of a conserved LPX motif (246–248; X = K in GLIC; *SI Appendix*, Fig. S1) in M2-M3, rotating K248 upward, from interaction with mostly D32(−) (preceding subunit) and E243 in the TMD in the O state, to interaction with D32 (same subunit) in the C state [as well as Y119 (β6–7/Cys loop), Y197 (M1) and E243]. Importantly, this rotation is coincident with L246 movement downward via a rigid LPK "wing nut" structure. L246 is bound in an aromatic cleft formed by the Cys loop (F116 and Y119) in the O state, but it detaches and binds to the TMD, behind M2, in the C state when the β-sandwich no longer offers a defined pocket (or it is occluded by P247). This movement apparently wedges closed the pore (Fig. 1*B*, *Right*), and is consistent with L246's high conservation and loss-of-function mutations in pLGICs (4). Moreover, L246 pushes into the allosteric intersubunit site for general anesthetics, suggesting a mechanism for receptor modulation from this site.

Closure of the TMD pore is well represented by the M2 radius, which decreases from ∼12.1 Å to 11.3 Å upon closing at low pH (Fig. 2*D* and *SI Appendix*, Fig. S4*F*), with the number of water molecules in the pore dropping from ∼38 to 0 (*SI Appendix*, Fig. S6*A*), as well as by M2-M1(−) distance, which undergoes a change from ∼13.5 Å to ∼17.5 Å (pH 7 is shown in *SI Appendix*, Fig. S4*E*). M2-M1(−) is a good subunit variable defining pore gating, undergoing a discrete change that involves loss of helical contacts between subunits (Fig. 2 *B* and *C*), although it also contributes to ECD-TMD twist via its tangential component. The TMD is slightly different in the optimized O state compared with PDB ID code 4HFI, being more open according to M2-M1(−) distance, which decreased from ∼14 Å to 13.5 Å, likely stabilizing M2-M1(−) packing, but similar or marginally reduced M2 radius. These changes during optimization may help explain difficulties in maintaining a wetted pore in microsecond-order simulations based on 4HFI/3EAM (34–36), whereas string simulations indefinitely maintain a wetted O state over 400 iterations.

Free-Energy Surfaces of Activation.
Illustration of receptor gating and pH modulation. We can use the large libraries of random transitions to calculate free-energy maps for coordinates of interest, without resorting to separate biased simulations. Doing so is possible because, after convergence, the path diffuses in a broad basin of low-energy configurations connecting the O and C states. We can summarize the gating process by calculating the free-energy as the function of one ECD variable, such as twist (ECD radius is shown in *SI Appendix*, Fig. S7*E*), and one TMD variable, such as M2-M1(−) distance (M2 radius is shown in *SI Appendix*, Fig. S8*E*, and pore hydration is shown in *SI Appendix*, Fig. S10 *A* and *B*), as shown in Fig. 4*A*. At low pH, there exists a curved path from the O state to the C state, requiring a highly twisted ECD to "unlock" the ECD before progressing to the C state, promoted by high pH. The map suggests an energy change of order $k_B T$ favoring the O state at pH 4.6, consistent with the experimental pH_{50} of 5.3 (4). At pH 7, the map is similar, but with the O state destabilized and a fully twisted intermediate (I_1) apparent. The I_1 state has expanded and twisted ECD, but features a semiopen (nonconducting) pore (*SI Appendix*, Table S1).

The O (PDB ID code 4HFI) and C (PDB ID code 4NPQ) structures are indicated with yellow and green points (one per subunit), respectively, in Fig. 4*A*. The relaxed O and C minima deviate from these structures due to optimization and the presence of membrane (and potentially the absence of detergent molecules in the upper pore). Based on M2-M1(−) alone, the O
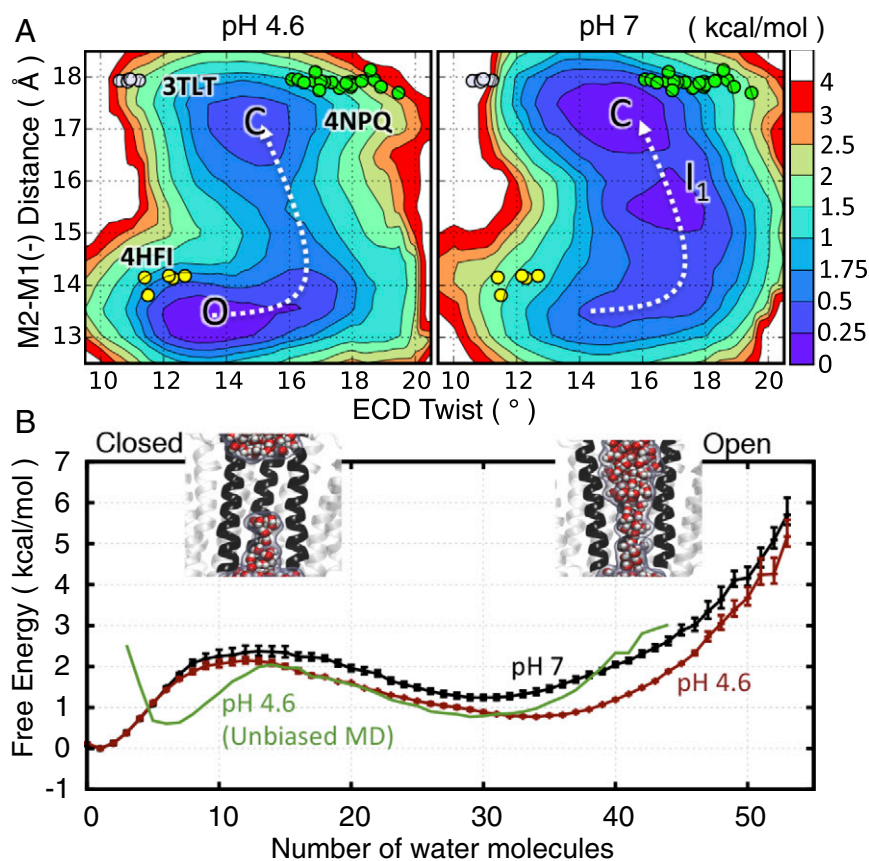
Fig. 4. (*A*) Free-energy maps showing M2-M1(−) distance against ECD twist for pH 4.6 (*Left*) and pH 7 (*Right*), with crystal subunit data shown as points [five points per structure; PDB ID code 4NPQ is shown with 20 points, corresponding to the four available structures (4)]. (*B*) One-dimensional free-energy profiles of hydration (pH 4.6 shown in red and pH 7 shown in black), with error bars as SDs. (*Insets*) Side views of the channel in the O/wetted and C/dewetted states. Superimposed is the un-biased estimate from limited free-simulation runs (green curve). Convergence is illustrated in *SI Appendix*, Fig. S6A.

pore is more open than 4HFI and the C state is less closed compared with 4NPQ. The ECD twist increased from 11° to 13° in 4HFI to 12° to 15° in the optimized O state (pH 4.6), whereas it decreased from 16° to 19° for 4NPQ to 13° to 16° in the optimized C state. The LC structure 3TLT (Fig. 4*A*, gray points) appears to the side of the broad basin, with an ECD twist of 11°. *SI Appendix*, Fig. S9 shows the rmsd to crystal structures, with the similarity to 4HFI for O changing to a similarity to 4NPQ for C, with a range of rmsds to LC along the path (discussed below).

The 1D free-energy profiles for water inside the pore (Fig. 4*B*) reveal a kilocalorie per mole order difference between the O (high hydration; Fig. 4*B*, *Right*) and C (low hydration; Fig. 4*B*, *Left*) states, and capture the anticipated pH shift, through increased probability of occupying the wetted state at pH 4.6 (Fig. 4*B*, red) relative to pH 7 (Fig. 4*B*, black). Integrating over O and C minima yields an O ⇌ C equilibrium constant change from 0.85 ± 0.03 at low pH to 2.0 ± 0.9 at high pH (i.e., favoring a wetted pore at low pH and a dewetted pore at high pH, and quantitatively demonstrating modulation by proton binding).

Quaternary ECD changes unlock the gating interface to enable an O-C transition. Fig. 5*A* shows the free-energy map for ECD radius versus lower β-expansion. At pH 4.6 (Fig. 5*A*, *Left*), a free-energy basin connects the O and C states via an intermediate, I_2, requiring significant spread of the ECD before the β-sandwich can expand to the C state. The fairly flat but orthogonal dependence suggests some decoupling of ECD and TMD changes, and a "binary switch" for sensing agonists, requiring ECD change above a threshold before a discrete conversion of the gating interface. In contrast, at high pH (Fig. 5*A*, *Right*), this threshold is mostly exceeded, leaving the channel to flicker between the I_2 and C states due to a dynamic β-sandwich.

These changes in the lower β-sandwich at the ECD–TMD interface lead to changes in the TMD, which we demonstrate by examining the free-energy projection involving β-expansion and M2-M1(−) in Fig. 5*B*. At low pH (Fig. 5*B*, *Left*), the broad

surface has two (left and right) pathways, with preference for the O state. Without ECD spread to cause β-expansion, the system would reside on the left side, with the pore flickering between the O and I_3 states. The LC 3TLT structure appears close to this intermediate, yet I_3, defined only by pore and β-sandwich variables, contains multiple clusters with wide-ranging ECD change (*SI Appendix*, Table S1). Two of these clusters have low rmsd to LC (3TLT), suggesting a relationship with this key intermediate. Thus, vertical movement between O and I_3 represents localized TMD pore closure, without the β-expansion needed to stabilize the C form. Such decoupled flickering of the pore is consistent with the coexistence of O and LC forms in a single crystal structure (4). The I_3 state helps close the channel in the presence of agonist, along the dominant left pathway. The less favored pathway is where the pore remains open, whereas the β-sandwich changes (right path), without the assistance of the I_3 state. Individual subunit maps (*SI Appendix*, Fig. S11) reveal that the converged string involves three subunits favoring the left path and two subunits favoring the right path, suggesting a degree of independence. We emphasize that maps for each subunit should not be the same but, when combined, as in Fig. 5*B*, should reveal what paths are possible.

At pH 7 (Fig. 5*B*, *Right*), the map is similar, favoring the dominant left pathway, with equilibrium shifted to states with greater M2-M1(−) (C). There are, in fact, multiple nonconducting states, including C, I_3, and two others with moderate M2-M1(−), that are visible in individual subunit maps (*SI Appendix*, Fig. S11) but averaged away in Fig. 5*B*, indicating some entropic stabilization of the nonconducting form. Because the ECD is more spread at pH 7, the probability of an expanded β-sandwich is increased, enabling lateral I_3-to-C exchange, shifting the equilibrium and leading to a dynamic protein, consistent with X-ray structural diversity (4).

Molecular interactions facilitate ECD–TMD communication. We can use free-energy projections to examine detailed molecular changes at

Lev et al.

www.manaraa.com
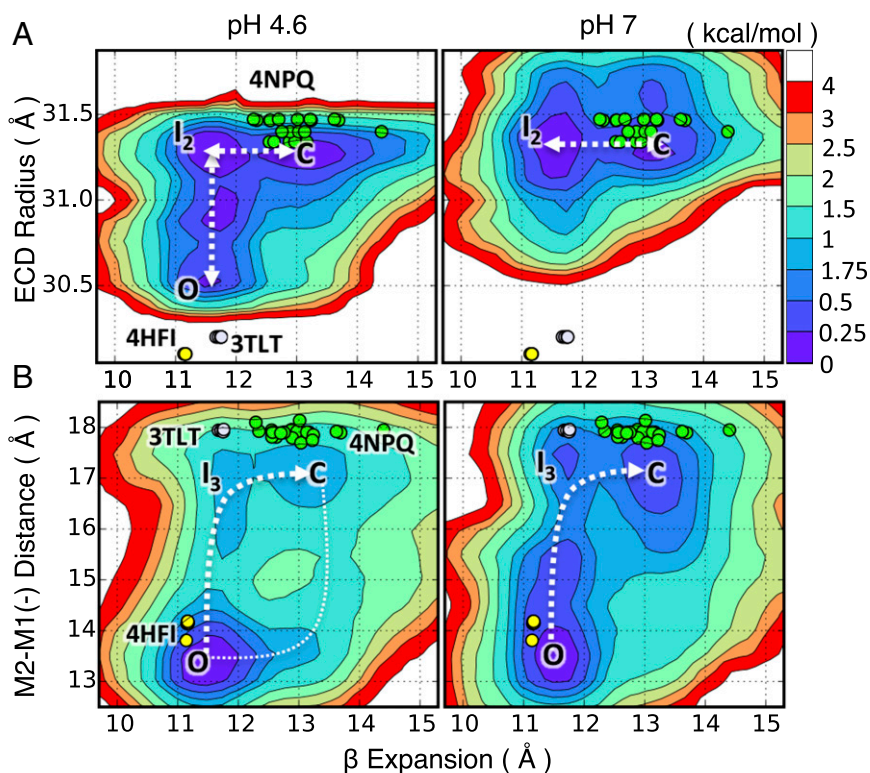
Fig. 5. (A) Free-energy maps showing β-expansion against ECD radius for pH 4.6 (*Left*) and pH 7 (*Right*). (*B*) Maps showing M2-M1(−) against β-expansion. Pathways are indicated with dashed lines, and crystal structure subunit data are shown as points.

the gating interface and how they relate to ECD and TMD changes. For example, relationships between β-expansion and pore closure can be seen involving the covalent linkage pre-M1, where breaking of D32-R192 displaces R192 (pre-M1), kinking M1 and inevitably altering the stability of the M2 that stacks upon it in the O state (Fig. 2*C*). *SI Appendix,* Fig. S12 shows maps for M1 kink against β-expansion and pore variables; for example, *SI Appendix,* Fig. S12*A* shows that M1 kink change occurs with β-expansion, whereas *SI Appendix,* Fig. S12 *B and C* illustrates how M1 kink adjustment is associated with pore closure. These dependencies are, however, subtle and do not necessarily imply communication is caused by pre-M1.

To examine the role of the M2-M3 LPK motif in ECD–TMD communication, we analyze the dependence of K248 distances to residues D32, D32(−), and E243 on β-expansion (*SI Appendix,* Fig. S13 *B–D*) and M2-M1(−) pore gating (*SI Appendix,* Fig. S14 *B–D*). On average (*SI Appendix,* Figs. S13 and S14, *Right*), K248 interacts more with D32(−) (as well as E243) in the O state, but then predominantly with D32 in the C state. The free-energy maps for pH 4.6 (*SI Appendix,* Figs. S13 and S14, *Left*) and pH 7 (*SI Appendix,* Figs. S13 and S14, *Center*) explain these trends, through increased probability of small D32 and large D32(−)/E243 distances as β-expansion or M2-M1(−) increases, escaping one minimum to move to another. This behavior appears independent of E243 protonation with pH, suggesting E243 interactions influence, but are not critical for, gating. We may use these maps to infer a role for K248 in interdomain communication; for example, *SI Appendix,* Fig. S13*B* shows that ECD β-expansion (freeing up D32) allows K248 to bind to D32 (not otherwise possible), whereas *SI Appendix,* Fig. S14*B* shows that K248 binding to D32 necessitates M2-M1(−) increase, and thus pore closure. Although not proof of causality (and maps show closure can occur without significant K248 movement), these results demonstrate the protein is constrained to follow this high-probability communication pathway. Mutation of K248 would eliminate its salt bridge to D32, and being stronger in the C state when D32 is available (and likely assists in breaking D32-R192), explains the gain-of-function phenotype seen experimentally in GLIC (K248C) (5).

We also analyze L246 binding to partners F116 (ECD) and F238 (TMD) against β-expansion (*SI Appendix,* Fig. S13 *E and F*) and M2-M1(−) pore gating (*SI Appendix,* Fig. S14 *E and F*). In *SI Appendix,* Figs. S13 *E and F, Right* and S14 *E and F, Right*, the panels show that, on average, L246 will exchange F116 with F238 (14′, interacting via V242) during gating, closing the pore by sterically interfering with M2, leading to dewetting (proven in *SI Appendix,* Fig. S15). To illustrate the L246 interdomain dependencies, *SI Appendix,* Fig. S13*E*, maps show that with low β-expansion, the protein prefers a minimum with large L246-F238 distance, but can escape to smaller L246-F238 distances with increased β-expansion. *SI Appendix,* Fig. S14*E* reveals that movement of L246 down toward F238 necessitates pore closure [increased M2-M1(−)]. This correlation, although also not necessarily causal, indicates that with high probability, the L246 is linked by both ECD and TMD gating changes.

Pore closure involves asynchronous initial M2 collapse. Fig. 2*D* suggested dewetting of the pore, correlated with M2 constriction and increased M2-M1(−) distance. M2 tangential and radial movements overall resemble an "iris"-like pore gating (see Movie S3), as suggested previously from a TMD-only model (37). However, individual subunit changes (pH 4.6 is shown in Fig. 6*A*) reveal that the most rapid change in M2-M1(−) occurs in the order of subunits B, C, D, A, and E. Although merely a guide, this tendency for some ordering is evident in all independent strings (*SI Appendix,* Fig. S3 *E–H*). To examine the nature of the subunit collapse better, we present the free energy as a function of M2 movement for subunit *n* and its neighbor *n* + 1 in Fig. 6*A*. Although the path is generally diagonal, suggesting some correlation of neighbor movements, the maps exhibit a degree of sequential collapse. We observe first a vertical movement from the O state as one helix experiences partial collapse from 13 Å to 15–16 Å, followed by diagonal movement as the helix and its neighbor collapse completely to a value of 17–18 Å. We can understand the influence of one subunit on the next by the interactions between M2-M1(−), as well as by intersubunit interactions via the M2-M3 loop. The work required to collapse the first helix partially is ~1 kcal/mol, whereas no work is required to complete the collapse of the helix and its neighbor

Lev et al.

www.manaraa.com
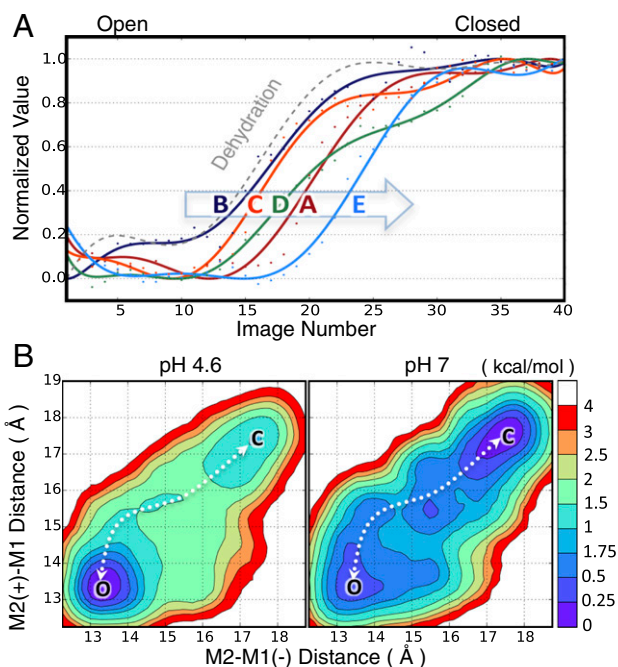
Fig. 6. (*A*) M2-M1(−) for five subunits (pH 4.6) illustrating asynchronous pore collapse (pH 7 is shown in *SI Appendix*, Fig. S3 *F* and *H*), with dehydration shown as a dashed gray curve for comparison. (*B*) Free-energy maps showing M2-M1(−) distance for the *n*th and *n*th + 1 subunits.

(being downhill). At high pH, the process has two stages, owing to a shallow intermediate with a half-collapsed M2 (as with I$_1$ in Fig. 4*A*). The partially sequential nature remains, but the cost is just ~$k_B T$, assisted by the intermediate and shifted toward the C state.

Although the relationship between pore hydration and size is simple (*SI Appendix*, Fig. S10*E*), *SI Appendix*, Fig. S10*D* reveals some orthogonal dependence on M2-M1(−), where change can occur without significant wetting/dewetting, still requiring activation (by ~2 kcal/mol), owing to the fact that pore hydration is potentially controlled by multiple subunits. However, dehydration superimposed in Fig. 6*A* (and *SI Appendix*, Fig. S3 *E–H*, gray curves) reveals that dewetting primarily occurs upon first M2 collapse, with the empty pore likely easing collapse of subsequent helices.

Wetting-dewetting transitions and unbiased observations. The pore hydration free energy in Fig. 4*B* can help explain the wetting-dewetting process. The O state (Fig. 4*B*, *Right*) consists of a broad well spanning 12–47 water molecules, centered on ~36 water molecules. The barrier is ~1.5 kcal/mol (relative to O, pH 4.6), occurring when the pore contains ~12 water molecules. We estimate that the Kramer's rate for dewetting at pH 4.6 is 11.4 μs^{-1} (transition every 88 ns; *SI Appendix*). The C state (Fig. 4*B*, *Left*) is narrow and deeper (higher wetting barrier of ~2.5 kcal/mol), conspiring to yield a similar Kramer's wetting rate of 12.2 μs^{-1} (transition every 82 ns). This result suggests that wetting and dewetting transitions from optimized states should happen on similar O(100 ns) time scales. At pH 7, the mean dewetting time is decreased twofold to 45 ns, consistent with rapid closing in unbiased simulations at pH 7 (38), whereas the wetting time is increased to 122 ns, which is expected, given the effect of pH on the equilibrium constant of gating above.

We have taken representative samples from the O-state minimum and launched independent unbiased simulations (Fig. 7*A*). In each case, the pore remains hydrated for some time before dewetting, with trajectories exhibiting repeated wetting-dewetting transitions on the order of 100-ns intervals. The occurrence of rewetting events is strong evidence for a stable O state. Projection onto maps for subunit changes [M2-M1(−) versus ECD twist and

β-expansion] in Fig. 7*B* shows good sampling around the O-state minimum and exploration of intermediate and C states. Select trajectories are shown in Fig. 7*C* (*Right*), with the graph demonstrating that transitions can follow the same two dominant pathways identified in our free-energy maps. Furthermore, the apparent onset of equilibrium in Fig. 7*A* suggests a reversible wetting-dewetting process, with an unbiased estimate of the free energy for hydration shown in Fig. 4*B* (green), having the same general shape as obtained from the string method, albeit with the C state not well sampled in limited free trajectories. These unbiased tests demonstrate a stable O state for GLIC, and that the identified pathways in string simulations are natural transitions of the protein.

Discussion and Conclusions

We have reported a string method optimization of the activation process for the GLIC ion channel, demonstrating modulated receptor function due to pH, revealing the pathways connecting stable O and C states via intermediates, and observing the communication mechanisms between agonist-binding ECD and ion-conducting TMD domains.

The key stimulus for gating is the protonation/deprotonation of residues that control ECD intersubunit interactions. We have made predictions for residues that generate force to spread or contract the ECD upon pH increase. Key titrated residues in our model are E35, E75, and E243, acting to close the channel at high pH (and thus, if mutated, would cause gain of function), with opposite effects from E26 and E177, acting to promote an O state at high pH (and thus, if mutated, would cause loss of function). The role of E177 suggests an interesting parallel to pLGICs that gate via agonist binding under loop C, whereas E75, at a pLGIC orthosteric site, highlights the role of loop A–B
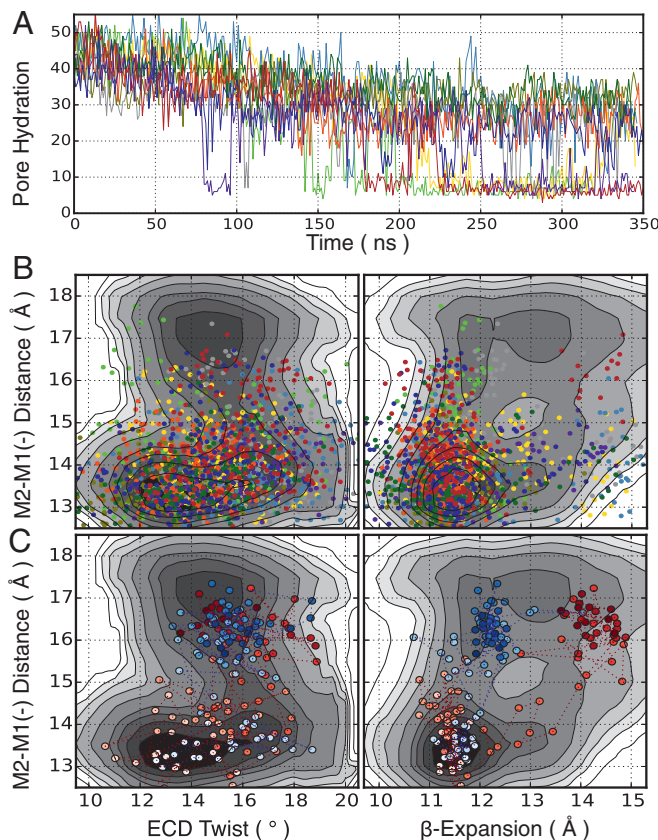
Fig. 7. Unbiased simulation from the optimized O state at pH 4.6. (*A*) Time series for pore hydration based on a set of ten 350-ns trajectories. (*B*) Superposition of trajectories on free-energy maps from Figs. 4 and 5. (*C*) Sample trajectories revealing unbiased sampling of different paths (color shaded by time).
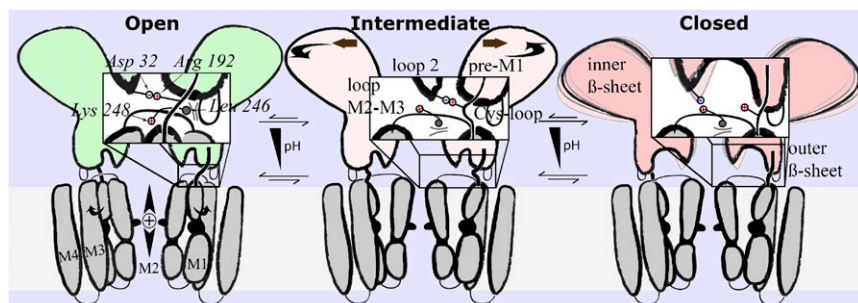
Fig. 8. Schematic of the gating mechanism. Interconversion of O and C states via an intermediate with a closed TMD pore but compact β-sandwich with a formed D32 (loop 2)-R192 (pre-M1) salt bridge. Upon expanding the lower β-sandwich to enter the C state, the LPK motif (M2-M3) flips, stabilized by K248 binding to D32, with L246 pushed down, closing the pore. (*Insets*) Gating interfaces. Arrows indicate an equilibrium shift to the C state with increased pH.

intersubunit interactions in gating and modulation. Residues close to the gating interface, such as E35 and E26, might play direct roles in β-sheet expansion; for example, E35 sits on β1-β2, packing against P247 on M2-M3 and contacting hydrophobic Cys loop and loop 9 residues from the adjacent subunit in the O state, which would be disfavored by protonation.

The result of deprotonation at high pH is to spread and twist the ECD, which are the leading events in channel closure, but the final steps in channel opening (Fig. 2*D*), consistent with the simulations of Cecchini and coworkers for GluCl (20) and analysis by Auerbach and coworkers for nAChR (39). We demonstrated that high levels of ECD twist are required along the gating pathway, making it an important variable for gating (39). Threshold levels of ECD spread alter the packing of subunits sufficiently to expand the lower β-sandwich around D32 (loop 2) and R192 (pre-M1), representing a binary switch mechanism for signal transduction. One interpretation is that the β-sandwich acts as an all-or-nothing switch that senses analog agonist signal to turn off or on the output electrical signal, as opposed to a gradual change that would be difficult to reconcile with the single conductance state seen experimentally (40).

Breaking of the D32-R192 salt bridge has consequences for the TMD. ECD–TMD coupling may occur via the pre-M1 linkage (30), where R192 movement can lead to M1 kinking, likely destabilizing its neighboring M2 in its O state (Fig. 2 *B* and *C*). We have, however, identified interesting β1-β2–M2-M3 loop interactions with strong interdomain dependencies that were not seen in GLIC crystal structures. K248 on M2-M3 is bound mostly within the TMD in the O state, but flips up to make contact with D32 in the C state, enabled by the freeing of D32 from R192 and the lining up of same-subunit residues through tangential twist. Although K248 has a corresponding R or K in the ELIC, GABA$_A$R, and GlyR subunits, it is lacking in GluCl, 5HT3 receptor, and nAChR (*SI Appendix,* Fig. S1), likely leading to variability. K248 is part of a well-conserved LPX motif (X = K in GLIC; *SI Appendix,* Fig. S1), with L246 stably bound in a hydrophobic cleft in the Cys loop in the O state, but driven into the TMD between M2 and M3 when the motif rotates, acting as a wedge to assist M2 collapse (Fig. 1*B* and Movie S1). Experiments introducing unnatural *cis*-proline have shown increased open probability in nAChRs (41), likely rotating the L246 equivalent upward. Importantly, in the C state, L246 sits adjacent to F14′, which occupies the pLGIC ethanol binding site, offering insight into how ethanol and anesthetic bromoform modulate pLGICs (42, 43). Our free-energy analysis has demonstrated strong connections between K248/L246 movements and both ECD and TMD changes, suggesting involvement in interdomain communication.

This communication thus centers on the changing availability of D32 during gating. D32 is part of a conserved triplet of interactions, with R192 maintaining interaction with D122 along the path (*SI Appendix,* Figs. S13*G* and S14*G*), and change involving only D32-R192 breakage (*SI Appendix,* Figs. S13*A* and S14*A*). D32E and D32N mutation both lower the pH$_{50}$ [by 0.7–1.5 (4)] and D32A leads to loss of activity (28), whereas in GlyR, the equivalent E53C reduces agonist sensitivity ~10-fold (27). D32 is conserved in GlyR, GABA$_A$R, nAChR, and 5HT3. In channels lacking a D32 equivalent (GluCl and ELIC in *SI Ap-*

pendix, Fig. S1), we cannot rule out roles for neighboring β1-β2 carboxylates, but postulate those channels might rely on pre-M1 communication, requiring the same β-sandwich expansion.

Our free-energy surfaces revealed flickering between O and nonconducting intermediate I$_3$, but that transfer to the C state requires β-expansion, driven by ECD change via intermediate I$_2$. To understand the relationship between I$_2$ and I$_3$, it is important to realize that a minimum on one free-energy projection may correspond to diverse configurations in another; for example, a minimum based on β-sandwich and pore variables could correspond to a whole distribution of ECD spread. Cluster analysis demonstrated related configurations for I$_2$ (from ECD spread—β-sandwich projection; Fig. 5*A*) and I$_3$ [from M2-M1(−)—β-sandwich projection; Fig. 5*B*] (*SI Appendix,* Table S1). Although I$_2$'s role is in maintaining a compact β-sandwich while spreading the ECD, the I$_3$ state exhibits a range of ECD change, yet with a common intact β-sandwich that represents the key intermediate gating feature (Fig. 8). I$_2$ and I$_3$ together represent a preactivated state in the C-O transition, consistent with the pLGIC "flip" kinetic state (44, 45), supported by the relationship between β1-β2 rearrangements and agonist efficacy in GlyR (46, 47), as well as by ϕ-analysis for the "conformational wave" of nAChR activation (48). The I$_2$ and I$_3$ states present a flipped LPK motif, associated with a closed pore, yet to be stabilized by interactions with the broken D32-R192 linkage (*SI Appendix,* Fig. S16). Two of the I$_3$ clusters have low rmsd to the proposed intermediate LC (C-like TMD, O-like ECD; *SI Appendix,* Table S2), suggesting that decoupling of ECD and TMD changes plays a role in gating, assisting closure in the presence of an agonist (26, 45, 49). At high pH, there is evidence for additional nonconducting states with semicollapsed M2 helices, implying entropically driven closure; for example, state I$_1$ (Fig. 4*A* and *SI Appendix,* Fig. S16) exhibits a semiclosed but nonconducting pore and transitional changes in the gating interface, indicated by L246 position, consistent with ϕ-analysis suggesting multistep M2 movements in nAChR (50).

During channel closure, M2 movements appear overall iris-like (37), yet exhibit a degree of asynchronous collapse, resembling a postulated "domino" mechanism (38, 51). Free-energy maps demonstrate that once the energy to collapse one subunit partially is paid, the neighboring subunit will fully collapse without further cost. We can understand this sequential nature from interactions between neighboring M2 and M1(−) and across the gating interface (involving M2-M3 and β1-β2) between subunits, as well as from the fact that pore dewetting occurs as a result of initial M2 collapse, assisting subsequent M2 movements. The partial or complete M2 movement would lead to a nonconducting pore, consistent with the lack of GLIC subconductance states (16, 40). In pLGICs with larger (e.g., GlyR 3JAE/F; *SI Appendix,* Fig. S8*E*) or more hydrophilic pores, however, partial movements could result in a semiconducting pore, as seen for GlyRs (52), modulated by interactions between M2-M1(−) (52, 53).

One might expect that these mechanisms would be largely shared within the pLGIC family, based on conservation of structures and residues, as well as the ability to form functional chimeras between GLIC and other members of the family (15, 54, 55). Available O and C high-resolution structures for GluCl and GlyR share dominant ECD and TMD pore movements and

www.manaraa.com

features at the gating interface, including interaction between D122 and R192 and M2-M3 loop displacement (3, 10, 20). However, comparisons shown in *SI Appendix*, Fig. S8, overlaying available structures on GLIC free-energy maps, suggest differences. For GluCl, changes between O (3RIA) and C (4TNV) are similar in terms of ECD radius, ECD twist, β-expansion, and M2 radius, although they exhibit reduced M2-M1(−) movement [previously noted (20)], perhaps due to the use of ivermectin to trap the GluCl O structure (3) or due to sequence differences in M2-M3 and β1-β2 loops. GlyR O (3JAE/F) and C (3JAD) structures reveal similar behavior for ECD twist and M2 radius (on an expanded scale), but with less β-expansion and markedly reduced ECD spread and M2-M1(−) distance [although this finding appears inconsistent with evidence for the interactions between M2-M1(−) that stabilize the GlyR O state (53)]. Differences are most prominent in the C state, for which GluCl and GlyR were stabilized by antibody fragments or the competitive inhibitor strychnine, although they may also be attributed to variability between cation- and anion-selective, or prokaryotic and eukaryotic channels.

The finding that the GLIC O-state structure is similarly open following optimization [with slight movement of M2 toward M1(−) to help stabilize the wetted pore], reinforces the fact that PDB ID code 4HFI (or PDB ID code 3EAM) corresponds to the O state, not artificially stabilized by detergent molecules, being absent in these simulations. Unbiased simulations confirm this stable state, with repeated rewetting transitions (not previously seen in simulations from crystal structures). We remark that optimization of the O state also leads to an E-2′ (bottom of M2) radius increase by ∼0.3 Å, with a lower M2 (−2′ to 9′) azimuthal rotation (10) away from 4HFI by ∼17°, acting to widen the lower pore. Although ∼1.2 Å less wide than the most open GlyR structure, it is over 1 Å wider than the collapsed form of that channel (10). Differences may be natural consequences of cation versus anion permeation, with Na$^+$ passing the constriction with the help of direct E-2′ coordination (as well as backbone) (14, 16), in contrast to Cl$^−$, which is expected to move as a hydrated ion past P-2′ in GlyR. These variations may suggest that although the current studies inform us of pLGIC allosteric mechanisms in general, detailed TMD changes may most directly relate to cationic members of the family.

In summary, we set out to understand GLIC channel activation using string method simulations and have made predictions for pH sensitivity and the interactions governing allosteric communication. We used free-energy analysis of swarms of trajectories to demonstrate GLIC modulation quantitatively by protons, consistent with experimental pH dependence (4), and solved for a stable O state, verified with unbiased MD simulation. Deprotonation of residues at the subunit interface drives ECD change during channel closure, consistent with observations for GluCl and nAChR (20, 39). Calculated forces have revealed the titrated residues responsible, including glutamates close to the gating interface likely to control β-sandwich change, on loop C [consistent with its role in pH sensitivity (33)] mimicking eukaryotic pLGICs, as well as at a conserved loop A ligand-binding site (26). We revealed a binary switch (β-sandwich expansion, D32-R192 breaking) that responds to threshold ECD change and directly communicates movement to the TMD. D32-R192 is part of a functionally important triplet (27, 28), with D32 mutation causing loss of function in GLIC and GlyR (4, 27, 28). The β-sandwich switching influences the TMD via the M2-M3 loop, which is important for function (9, 10, 20, 28) and identified in nAChR activation (39). A conserved LPX (L246, P247, and K248 in GLIC) motif flips to engage D32 in the expanded β-sandwich, driving L246 [essential for pLGIC function (4)] down toward a general anesthetic site (42, 43) to force the pore closed. P247 is important in nAChRs (41), and our observations for K248 explain its experimental mutant phenotypes in GLIC (5). Our independently solved intermediate with a closed pore and compact β-sandwich includes an LC-like form seen experimentally (5), and provides a low-energy path in the presence of agonist, consistent with the "preactive" (26) or flip (45, 49) pLGIC state. We observe

iris-like M2 movements, consistent with studies of a TMD-only channel (37), but modulated by the gating interface, leading to asynchronous movements involving partial collapse. Identification of a partially closed state is consistent with φ-analysis in nAChRs (50), and may explain subconductance states in channels such as GlyR (52). We see similarities to other pLGIC gating movements, with ECD change, β-sandwich switching, and pore collapse conserved, yet warranting separate string method investigations.

pLGICs are primary targets for general anesthetics (56), as well as for drugs that treat acquired or inherited mutations responsible for diseases such as epilepsy (57). The results of this study improve our knowledge of pLGIC function, revealing details of the molecular events during gating intimately involved with anesthetic and drug-binding sites. The string method, with transition analysis, has been proven to capture receptor modulation by protons, in addition to stable O, C, and intermediate states that may be tested with experimental trapping or emerging time-resolved structural methods (58), providing potential new targets for therapeutic drugs.

Methods

The GLIC protein in the O and C states [PDB ID codes 4HFI (16) and 4NPQ (4), respectively] were embedded in bilayers of 1-palmitoyl-2-oleoyl-sn-glycero-3-phosphocholine with explicit TIP3P water and 150 mM NaCl, totalling 150,235 atoms. Systems were built and preequilibrated with CHARMM (59), and simulated using NAMD (60) with the CHARMM36 force field (61–64). Additional unbiased/free-trajectory simulations using GROMACS 4.6.6 (13) with the CHARMM36 force field are also described in *SI Appendix*. Ionization states for pH 4.6 (activated) and pH 7 (closed/resting) were based on pK$_a$ estimates, mutagenesis, and crystallographic data (6). At low pH, the sites of protonation were E26, E35, E67, E69, E75, E82, E177, E243, and H277, as indicated in Fig. 1A, whereas standard states were used at pH 7, with the exception of H127, which was protonated at both pH values (*SI Appendix*).

We first ran rmsd-based targeted MD to generate guess paths between the O and C states at each pH (*SI Appendix*). Independent strings were initiated by exchanging structures between pH values. We then carried out a string method approach, based on the swarms of trajectories method (23–25), requiring definition of a lower dimensional space. We chose the following variables for each of the five subunits (35 in total; definitions are provided in *SI Appendix*): ECD twist, ECD upper and lower spread (two variables; however, for analysis, we analyze one upper "ECD radius"; *SI Appendix*), lower β-sandwich expansion ("β-expansion," distance between β-sheets in the vicinity of D32 and R192), M2-M1(−) distance, upper M2 spread (reported as "M2 radius"), and M1 kink at conserved P204 (Fig. 2). All variables have been normalized to ensure equal weight in the optimization. Other interesting coordinates, such as ECD–TMD separation, subunit, and helical tilting, were well correlated with these variables (select correlations are illustrated in *SI Appendix*, Fig. S2, based on initial optimizations described in *SI Appendix*).

Forty image structures (plus two fixed end points) were sampled uniformly along the targeted MD trajectory for each pH. We refined these structures using a swarm of 20 short (10-ps) simulations launched from each image. Images were updated based on mean drift in each swarm, redistributing between end states and relaxing with 20-ps constrained simulations. At least 400 iterations were completed for each string. We acknowledge that the degree and order of changes could be influenced by the initial trajectory in the event of a lack of convergence. *SI Appendix*, Fig. S17 demonstrates convergence within 300 iterations (last 100 analyzed), with similar changes in all four independent strings (*SI Appendix*, Fig. S3 A–D).

We constructed free-energy maps in spaces defined by a selection of variables, X, using unbiased swarm trajectories after convergence via a transition analysis similar to Markov state modeling (e.g. ref. 65) not previously applied to string method solutions. To obtain the probability that the system occupies point k in this space, $\rho_k(X)$, we computed the dimensionless transition probability P_{kl}, from a transition count matrix, normalized by source to remove bias from image locations. We sought a stationary solution for $\rho_k(t)$ by iterating the discretized master equation:

$$\rho_k(t + \delta t) = \rho_k(t) + \sum_{l \neq k} [\rho_l(t) P_{lk} - \rho_k(t) P_{kl}],$$

from which we computed the potential of mean force, $W_k = -k_B T \ln(\rho_k)$. W_k corresponds to an equilibrium free-energy projection, where remaining coordinates are sampled within the broad basin around the string. Maps were calculated from analysis of different subunit variables (whole-pentamer results

www.manaraa.com

are shown in *SI Appendix*, Fig. S18), revealing interdependencies related to channel gating. Other free-energy profiles were obtained by mean force or constraint force integration, solving the Poisson–Boltzmann equation to estimate electrolyte screening, with full details provided in *SI Appendix*.

1. Changeux JP (2012) Allostery and the Monod-Wyman-Changeux model after 50 years. *Annu Rev Biophys* 41:103–133.
2. Cecchini M, Changeux JP (2015) The nicotinic acetylcholine receptor and its prokaryotic homologues: Structure, conformational transitions and allosteric modulation. *Neuropharmacology* 96:137–149.
3. Hibbs RE, Gouaux E (2011) Principles of activation and permeation in an anion-selective Cys-loop receptor. *Nature* 474:54–60.
4. Sauguet L, et al. (2014) Crystal structures of a pentameric ligand-gated ion channel provide a mechanism for activation. *Proc Natl Acad Sci USA* 111:966–971.
5. Prevost MS, et al. (2012) A locally closed conformation of a bacterial pentameric proton-gated ion channel. *Nat Struct Mol Biol* 19:642–649.
6. Bocquet N, et al. (2009) X-ray structure of a pentameric ligand-gated ion channel in an apparently open conformation. *Nature* 457:111–114.
7. Hilf RJ, Dutzler R (2009) Structure of a potentially open state of a proton-activated pentameric ligand-gated ion channel. *Nature* 457:115–118.
8. Hilf RJ, Dutzler R (2008) X-ray structure of a prokaryotic pentameric ligand-gated ion channel. *Nature* 452:375–379.
9. Althoff T, Hibbs RE, Banerjee S, Gouaux E (2014) X-ray structures of GluCl in apo states reveal a gating mechanism of Cys-loop receptors. *Nature* 512:333–337.
10. Du J, Lü W, Wu S, Cheng Y, Gouaux E (2015) Glycine receptor mechanism elucidated by electron cryo-microscopy. *Nature* 526:224–229.
11. Huang X, Chen H, Michelsen K, Schneider S, Shaffer PL (2015) Crystal structure of human glycine receptor-α3 bound to antagonist strychnine. *Nature* 526:277–280.
12. Hassaine G, et al. (2014) X-ray structure of the mouse serotonin 5-HT3 receptor. *Nature* 512:276–281.
13. Miller PS, Aricescu AR (2014) Crystal structure of a human GABAA receptor. *Nature* 512:270–275.
14. Morales-Perez CL, Noviello CM, Hibbs RE (2016) X-ray structure of the human α4β2 nicotinic receptor. *Nature* 538:411–415.
15. Duret G, et al. (2011) Functional prokaryotic-eukaryotic chimera from the pentameric ligand-gated ion channel family. *Proc Natl Acad Sci USA* 108:12143–12148.
16. Sauguet L, et al. (2013) Structural basis for ion permeation mechanism in pentameric ligand-gated ion channels. *EMBO J* 32:728–741.
17. Dellisanti CD, et al. (2013) Site-directed spin labeling reveals pentameric ligand-gated ion channel gating motions. *PLoS Biol* 11:e1001714.
18. Nury H, et al. (2011) Conformational dynamics in a nicotinic receptor homologue probed by simulations. *Biophys J* 100:272.
19. Yu R, et al. (2014) Agonist and antagonist binding in human glycine receptors. *Biochemistry* 53:6041–6051.
20. Calimet N, et al. (2013) A gating mechanism of pentameric ligand-gated ion channels. *Proc Natl Acad Sci USA* 110:E3987–E3996.
21. Yoluk Ö, Lindahl E, Andersson M (2015) Conformational gating dynamics in the GluCl anion-selective chloride channel. *ACS Chem Neurosci* 6:1459–1467.
22. Orellana L, Yoluk O, Carrillo O, Orozco M, Lindahl E (2016) Prediction and validation of protein intermediate states from structurally rich ensembles and coarse-grained simulations. *Nat Commun* 7:12575.
23. Weinan E, Ren WQ, Vanden-Eijnden E (2002) String method for the study of rare events. *Phys Rev E* 66:052301.
24. Pan AC, Sezer D, Roux B (2008) Finding transition pathways using the string method with swarms of trajectories. *J Phys Chem B* 112:3432–3440.
25. Zhao C, Noskov SY (2013) The molecular mechanism of ion-dependent gating in secondary transporters. *PLOS Comput Biol* 9:e1003296.
26. Corringer PJ, et al. (2012) Structure and pharmacology of pentameric receptor channels: From bacteria to brain. *Structure* 20:941–956.
27. Pless SA, Leung AW, Galpin JD, Ahern CA (2011) Contributions of conserved residues at the gating interface of glycine receptors. *J Biol Chem* 286:35129–35136.
28. Bertozzi C, Zimmermann I, Engeler S, Hilf RJC, Dutzler R (2016) Signal transduction at the domain interface of prokaryotic pentameric ligand-gated ion channels. *PLoS Biol* 14:e1002393.
29. Lee WY, Sine SM (2005) Principal pathway coupling agonist binding to channel gating in nicotinic receptors. *Nature* 438:243–247.
30. Purohit P, Auerbach A (2007) Acetylcholine receptor gating at extracellular transmembrane domain interface: The "pre-M1" linker. *J Gen Physiol* 130:559–568.
31. Dellisanti CD, Hanson SM, Chen L, Czajkowski C (2011) Packing of the extracellular domain hydrophobic core has evolved to facilitate pentameric ligand-gated ion channel function. *J Biol Chem* 286:3658–3670.
32. Bali M, Akabas MH (2007) The location of a closed channel gate in the GABAA receptor channel. *J Gen Physiol* 129:145–159.
33. Wang H-L, Cheng X, Sine SM (2012) Intramembrane proton binding site linked to activation of bacterial pentameric ion channel. *J Biol Chem* 287:6482–6489.
34. LeBard DN, Hénin J, Eckenhoff RG, Klein ML, Brannigan G (2012) General anesthetics predicted to block the GLIC pore with micromolar affinity. *PLOS Comput Biol* 8:e1002532.
35. Laurent B, Murail S, Da Silva F, Corringer P-J, Baaden M (2012) Modeling complex biological systems: From solution chemistry to membranes and channels. *Pure Appl Chem* 85:1–13.
36. Willenbring D, Liu LT, Mowrey D, Xu Y, Tang P (2011) Isoflurane alters the structure and dynamics of GLIC. *Biophys J* 101:1905–1912.
37. Zhu F, Hummer G (2010) Pore opening and closing of a pentameric ligand-gated ion channel. *Proc Natl Acad Sci USA* 107:19814–19819.
38. Nury H, et al. (2010) One-microsecond molecular dynamics simulation of channel gating in a nicotinic receptor homologue. *Proc Natl Acad Sci USA* 107:6275–6280.
39. Gupta S, Chakraborty S, Vij R, Auerbach A (2017) A mechanism for acetylcholine receptor gating based on structure, coupling, phi, and flip. *J Gen Physiol* 149:85–103.
40. Bocquet N, et al. (2007) A prokaryotic proton-gated ion channel from the nicotinic acetylcholine receptor family. *Nature* 445:116–119.
41. Lummis SC, et al. (2005) Cis-trans isomerization at a proline opens the pore of a neurotransmitter-gated ion channel. *Nature* 438:248–252.
42. Sauguet L, et al. (2013) Structural basis for potentiation by alcohols and anaesthetics in a ligand-gated ion channel. *Nat Commun* 4:1697.
43. Laurent B, et al. (2016) Sites of anesthetic inhibitory action on a cationic ligand-gated ion channel. *Structure* 24:595–605.
44. Lape R, Colquhoun D, Sivilotti LG (2008) On the nature of partial agonism in the nicotinic receptor superfamily. *Nature* 454:722–727.
45. Sivilotti LG (2010) What single-channel analysis tells us of the activation mechanism of ligand-gated channels: The case of the glycine receptor. *J Physiol* 588:45–58.
46. Pless SA, Lynch JW (2009) Magnitude of a conformational change in the glycine receptor beta1-beta2 loop is correlated with agonist efficacy. *J Biol Chem* 284:27370–27376.
47. Soh MS, Estrada-Mondragon A, Durisic N, Keramidas A, Lynch JW (2017) Probing the structural mechanism of partial agonism in glycine receptors using the fluorescent artificial amino acid, ANAP. *ACS Chem Biol* 12:805–813.
48. Purohit P, Gupta S, Jadey S, Auerbach A (2013) Functional anatomy of an allosteric protein. *Nat Commun* 4:2984.
49. Burzomato V, Beato M, Groot-Kormelink PJ, Colquhoun D, Sivilotti LG (2004) Single-channel behavior of heteromeric alpha1beta glycine receptors: An attempt to detect a conformational change before the channel opens. *J Neurosci* 24:10924–10940.
50. Purohit P, Mitra A, Auerbach A (2007) A stepwise mechanism for acetylcholine receptor channel gating. *Nature* 446:930–933.
51. Duke TA, Le Novère N, Bray D (2001) Conformational spread in a ring of proteins: A stochastic approach to allostery. *J Mol Biol* 308:541–553.
52. Rajendra S, et al. (1995) Mutation of an arginine residue in the human glycine receptor transforms beta-alanine and taurine from agonists into competitive antagonists. *Neuron* 14:169–175.
53. Bode A, Lynch JW (2013) Analysis of hyperekplexia mutations identifies transmembrane domain rearrangements that mediate glycine receptor activation. *J Biol Chem* 288:33760–33771.
54. Eiselé JL, et al. (1993) Chimaeric nicotinic-serotonergic receptor combines distinct ligand binding and channel specificities. *Nature* 366:479–483.
55. Grutter T, et al. (2005) Molecular tuning of fast gating in pentameric ligand-gated ion channels. *Proc Natl Acad Sci USA* 102:18207–18212.
56. Nury H, et al. (2011) X-ray structures of general anaesthetics bound to a pentameric ligand-gated ion channel. *Nature* 469:428–431.
57. Reid CA, Berkovic SF, Petrou S (2009) Mechanisms of human inherited epilepsies. *Prog Neurobiol* 87:41–57.
58. Schwoerer H, Chapman HN, Siwick BJ, Miller RJD (2016) Special issue on imaging the dynamic structure of matter. *J Phys At Mol Opt Phys* 49:150201.
59. Brooks BR, et al. (2009) CHARMM: The biomolecular simulation program. *J Comput Chem* 30:1545–1614.
60. Phillips JC, et al. (2005) Scalable molecular dynamics with NAMD. *J Comput Chem* 26:1781–1802.
61. MacKerell AD, et al. (1998) All-atom empirical potential for molecular modeling and dynamics of proteins. *J Phys Chem B* 102:3586–3616.
62. Mackerell AD, Jr, Feig M, Brooks CL, 3rd (2004) Extending the treatment of backbone energetics in protein force fields: Limitations of gas-phase quantum mechanics in reproducing protein conformational distributions in molecular dynamics simulations. *J Comput Chem* 25:1400–1415.
63. Klauda JB, et al. (2010) Update of the CHARMM all-atom additive force field for lipids: validation on six lipid types. *J Phys Chem B* 114:7830–7843.
64. Jorgensen WL, Chandrasekhar J, Madura JD, Impey RW, Klein ML (1983) Comparison of simple potential functions for simulating liquid water. *J Chem Phys* 79:926–935.
65. Buch I, Giorgino T, De Fabritiis G (2011) Complete reconstruction of an enzyme-inhibitor binding process by molecular dynamics simulations. *Proc Natl Acad Sci USA* 108:10184–10189.

Lev et al.

www.manaraa.com